ADVANCED OPTICAL MATERIALS
www.advopticalmat.de

Self-Aligned Waveguide Array Integrated with Flat Microlenses for Environment-Adaptive and High-Resolution Compound Eye Vision

Hyuk Jae Jang, Ji-Eun Yeo, Gil Ju Lee, Hoon Hahn Yoon,* and Young Min Song**

While recent advances in artificial compound-eye vision systems have demonstrated environmental adaptability, the precise control and optimization of the light collection with achieving high-resolution (HR) through self-aligned waveguides (WGs) remain a critical challenge. High-density integration of flat microlens (fML) array using optimized self-aligned light waves is promising, but practical implementation requires a detailed understanding of fabrication parameters and optical mechanisms. Here, an artificial compound eye system is presented that combines a fML array with a self-aligned WG to achieve stable, HR imaging across the air and underwater environments. Unlike conventional curved microlenses, the fML design maintains consistent optical properties across environments, while self-aligned WGs ensure efficient light collection through precisely positioned channels beneath each microlens. The optical simulations and experimental verification demonstrate stable optical properties over a wide range of refractive indices and optimized light guidance through the optical WG. This novel integration scheme presented in this work, which enables high density while maintaining environmental adaptability for efficient light collection, opens new possibilities for compact vision systems in various applications ranging from underwater imaging to biomedical sensing.

1. Introduction

In nature, animal vision systems have evolved to adapt to diverse and challenging environments, giving rise to specialized visual capabilities that support survival and functionality in specific habitats. These visual capabilities include amphibious vision, high-resolution (HR) vision, a wide field of view (FoV), sensitivity to ultraviolet (UV) and infrared light, polarized light detection, and efficient depth estimation.[1–12] Certain species have evolved among these adaptations to possess amphibious features efficiently, enabling vision compatible with aquatic and terrestrial environments.[13–17] Generally, natural focusing lenses have a curved shape, which is commonly employed in artificial cameras, including human-eye-type (designed for terrestrial environments),[9,18–20] insect-eye-type (terrestrial),[2,21] and fish-eye-type (aquatic)[1,3] artificial vision systems. However, the fiddler crab, inhabiting intertidal regions, uniquely utilizes a flat lens to maintain visual information across the air and underwater environments.[17,22–23] This adaptation provides optical stability during refractive index (RI) transitions between air and water, as flat lenses minimize focal length shifts by maintaining constant transmitted angle and focusing light through RI distribution within the inner part of the lens, rather than relying on outer surface curvature and RI—a contrast to curved lenses, where changes in surface geometry and RI result in variable refraction and focusing, as described by Snell's law and the lens maker's principle. An amphibious camera with panoramic vision has been developed, inspired by the fiddler crab's amphibious vision and extremely wide FoV, which is achieved through the geometrical arrangement of optical units known as ommatidia.[4]

A compound eye typically consists of hundreds to thousands of ommatidia, each functioning as an independent optical system. The ommatidium in an apposition-type compound eye consists of a facet lens, crystalline cone, rhabdom, and photoreceptor

H. J. Jang, J.-E. Yeo, Y. M. Song
School of Electrical Engineering and Computer Science
Gwangju Institute of Science and Technology (GIST)
Cheomdangwagi-ro 123, Buk-gu, Gwangju 61005, Republic of Korea
E-mail: ymsong@gist.ac.kr

The ORCID identification number(s) for the author(s) of this article can be found under https://doi.org/10.1002/adom.202500926

DOI: 10.1002/adom.202500926

G. J. Lee
School of Electrical and Electronics Engineering
Pusan National University
2, Busandaehak-ro 63, Geumjeong-gu, Busan 46241, Republic of Korea
E-mail: gjlee0414@pusan.ac.kr

H. H. Yoon, Y. M. Song
Department of Semiconductor Engineering
Gwangju Institute of Science and Technology (GIST)
Cheomdangwagi-ro 123, Buk-gu, Gwangju 61005, Republic of Korea
E-mail: hoonhahnyoon@gist.ac.kr

Y. M. Song
Artificial Intelligence (AI) Graduate School
Gwangju Institute of Science and Technology (GIST)
Cheomdangwagi-ro 123, Buk-gu, Gwangju 61005, Republic of Korea

cell. The facet lens and crystalline cone refract light to efficiently channel light toward the rhabdom and photoreceptor cell, which are specialized for light detection.[24] To replicate these beneficial optical characteristics, the structural and functional biomimicry of the natural ommatidia using microlenses (MLs) has been explored. 3D printing techniques have been employed to create artificial apposition-type compound eyes.[25] Alternatively, polymer-based ML arrays-assisted with a 3D isolation layer, have been developed to reduce optical crosstalk between lenses, thus mimicking natural compound eyes' structural and functional features.[12] However, these methods often involve complex fabrication processes, and scaling down the ML size to achieve a compact HR vision system remains a significant challenge.[12,25] One approach to overcoming these limitations is to utilize MLs to cure a polymer, achieving a self-aligned waveguide (WG) based on the RI difference between photo-crosslinked and thermal-crosslinked polymers.[11,26–28] These methods have realized the compact artificial compound eye, but previous efforts to imitate the natural ommatidium have focused on the fabrication process and simple demonstration in air condition using curved microlens (cML). Furthermore, thus far, self-aligned WGs typically use cML, which lose optical performance when RI changes in the surrounding environment (e.g., air and water conditions) affect the focusing power of the ML.[29] In such designs, the photo-cured WGs inherently inherit the optical instability of cMLs due to focal length variations under RI shifts. In contrast, by integrating the UV-curing process with flat microlens (fML)—whose focusing behavior remains stable across air and water—we achieve WGs that maintain consistent guiding performance regardless of the external environment. This configuration enables the formation of a universal, amphibious optical pathway, representing a significant advancement in WG-based compound eye vision systems. While recent work has demonstrated environmental adaptability using a fML array,[4] the integration of self-aligned WGs with such systems—which could enhance light collection efficiency and enable more compact and HR vision designs with one-shot imaging capability without complex post-processing, such as a scanning method—has remained unexplored due to fabrication challenges.

To address these limitations of current fML systems and expand upon previous work, our study provides a comprehensive analysis and optimization of self-aligned WG formation with a highly integrated fML array. This work overcomes these limitations and focuses on several critical aspects: 1) successful high-density integration of self-aligned WGs with fMLs through optimized UV exposure parameters, a significant advancement over previous bulk spacer designs, 2) quantitative analysis of RI gradients and their impact on optical performance, 3) detailed characterization of light propagation mechanisms in environment-adaptive self-aligned WGs formation using fML, 4) optimization guidelines for practical fabrication parameters and validation for HR imaging capabilities, and 5) experimental imaging demonstration of the environment-adaptive HR vision using miniaturized fML with amphibious self-aligned WG. Our approach enables precise and automatic formation of WGs beneath each ML through carefully controlled UV exposure of photosensitive polymer resin, significantly simplifying the fabrication process while enhancing optical performance.

Unlike conventional cML approaches, our system utilizes fMLs that maintain consistent optical performance across various RI environments (e.g., air and water). While previous designs with bulk spacers also achieved environmental adaptability, our integration of self-aligned WGs with fMLs significantly enhances light collection efficiency, enabling more compact and HR imaging device architectures. Through comprehensive optical simulations and experimental validation, we demonstrate that our fML-based self-aligned WG system not only maintains the stable focal performance of previous designs but also provides superior light guidance through precise WG formation. The successful integration of self-aligned WGs with fMLs represents a significant advance in fabrication approach and optical performance for amphibious vision systems. This development opens new possibilities for compact HR vision systems in dynamic environments, with potential applications ranging from medical monitoring to autonomous navigation.

2. Results and Discussion

2.1. Concept of Environment-Adaptive and HR Artificial Compound Eye (ACE)

In nature, organisms have evolved specialized visual adaptations to enhance survival in diverse environments. Among these adaptations, amphibious vision enables species such as the fiddler crab to maintain stable visual perception in both terrestrial and aquatic conditions (**Figure 1a**). By mimicking these amphibious natural compound eyes, the development of an amphibious ACE system enables the creation of environment-adaptive imaging devices suitable for various dynamic environments.

Figure 1b presents a detailed comparison of natural ommatidium's optical and structural properties for the fML and cML systems as applied to designing an amphibious artificial compound eye. The structural design of the artificial ommatidium was inspired by natural compound eyes found in both terrestrial/aquatic species and semiterrestrial species. These compound eyes vary in nature based on environmental adaptations, with terrestrial/aquatic species generally having curved corneal lenses and semiterrestrial species, such as the fiddler crab, having flat corneal lenses. Cross-sectional schematics of the artificial ommatidium reveal how the cML and fML systems with WG function differently in air and underwater environments. Optical ray paths, depicted in green (air) and blue (underwater), show that the focusing power of the cML system diminishes underwater. In contrast, the fML system maintains a stable focus across both environments.

The resolution of an artificial compound eye system, i.e., the image quality, is fundamentally determined by the number of MLs and the light collection efficiency. In conventional cML systems, RI variations between air and underwater degrade image resolution and intensity. Figure 1c illustrates the imaging qualities of ML types and density on imaging performance using optical simulation software, comparing a low-density cML array (10 × 10 MLs) with a high-density fML array (30 × 30 MLs). The

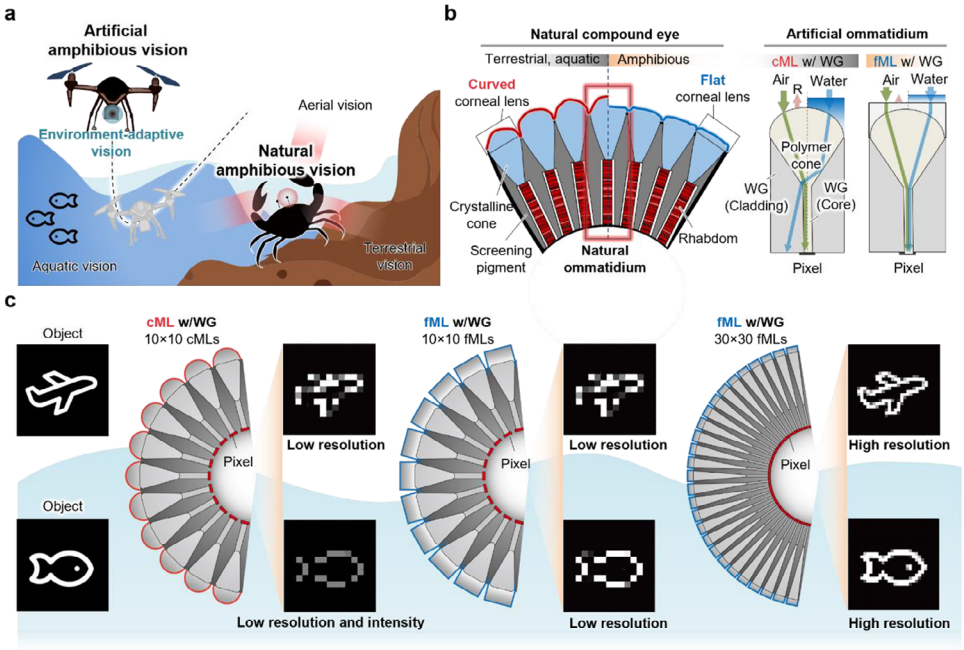

Figure 1. Concept of amphibious HR ACE vision system inspired by the natural compound eye of the fiddler crab. a) Comparison between natural amphibious compound eye vision (e.g., fiddler crab eye) and artificial amphibious vision. b) Structural comparison of curved and flat lenses between natural ommatidium and artificial ommatidium. c) Image simulation of environment-adaptive and HR ACE with a highly integrated fML array with WG. The resolution and light intensity of the reconstructed image depend on the number of MLs. The cML system results in LR and reduced intensity in aquatic environment, while the fML system achieves the amphibious imaging capabilities. Furthermore, the integration of fML with WG enhances a highly integrated fML system by enabling precise control of optical system design, such as total track length, system volume, and focal length while maintaining optical efficiency.

resolution and light intensity of the reconstructed image are influenced by multiple factors, including ML array density, individual lens diameter, and WG length. Among these, the dominant contributor to resolution enhancement is the increased array density, which improves spatial sampling. The reduction in ML size also contributes by increasing angular resolution, but its impact is secondary to the array densification in this system design.

The low-density cML system suffers from low resolution (LR) and reduced light intensity, as individual MLs cannot efficiently propagate light to the imaging plane. Furthermore, when submerged in water, the focal length shift of cMLs is larger than that of fML, further reducing imaging stability. In contrast, the fML with WG system maintains consistent focusing power across different environments, enabling stable imaging quality in multi-environments. In particular, integrating an amphibious self-aligned WG can realize a highly integrated HR imaging device. Furthermore, highly integrated fML-WG arrays that enable highly integrated fML array configurations can significantly increase the total pixel count and spatial resolution of imaging systems based on artificial compound vision. As shown in Figure 1c, increasing the number of MLs results in a sharper and more detailed reconstructed image, highlighting the superior resolution capability of the fML-WG system. In addition, the precise alignment between fMLs and self-aligned WGs enhances light confinement, minimizing optical losses and improving image clarity.

2.2. Fabrication and Optical Analysis of fML Array with Self-Aligned WG Formation

Figure 2a exhibits the fabrication process of the fML array with self-aligned WG. The fabrication of the polydimethylsiloxane (PDMS) mold used to construct the fML array is described in the Experimental Section and Figure S1 (Supporting Information). The fabrication process begins with surface treatment of PDMS mold, followed by O_2 plasma treatment and hydro-coating at 4000 rpm for 30 s to facilitate demolding SU-8. Next, SU-8 2100 is spin-coated onto the PDMS mold at 1500 rpm for 30 s. This first coating is cured by a soft baking process on a hot plate at 65 °C for 7 min for stable heat transfer. A second layer of SU-8 2100 is then spin-coated under the same conditions for sufficient SU-8 membrane thickness (Figure S2, Supporting Information), followed by another soft bake. Subsequently, both layers are baked at 95 °C in a convection oven for 3 h to ensure stability. After the SU-8 cML array is prepared, the SU-8 cML array is treated with O_2 treatments. Norland optical adhesive (NOA) 1369 is then spin-coated at 4000 rpm for 30 s and pre-cured with UV irradiation (365 nm; 1000 mJ cm^{-2}) for a rigid state. The sample is then exposed to UV light for different durations (260, 520, 780, 1040, 1300, and 1560 mJ cm^{-2}) to initiate curing. Finally, post-exposure baking is performed for thermal-crosslinking in two stages: first at 65 °C for 5 min, followed by 20 min at 95 °C, completing the curing process for the SU-8 layers.

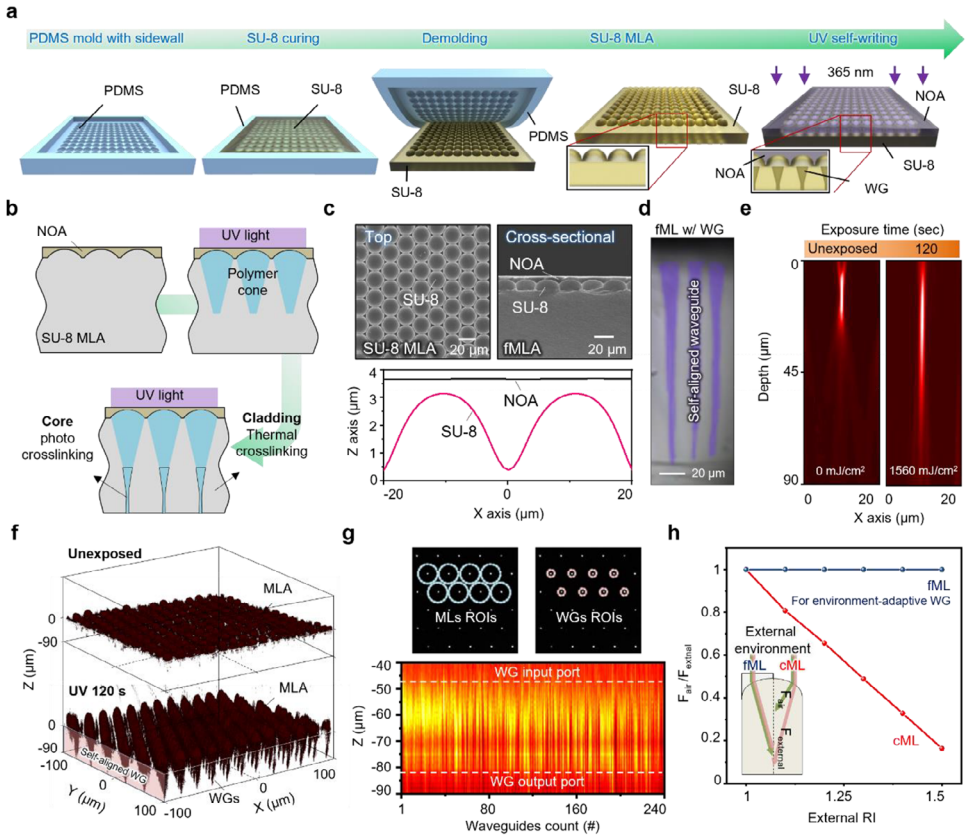

Figure 2. Fabrication process and optical/structural analysis of fML array with self-aligned WG formation. a) Schematic illustration of the fML array fabrication process using SU-8 and NOA. The fML array is fabricated with PDMS mold preparation, SU-8 curing, demolding, and NOA coating. The self-aligned WGs in fML array are formed via UV light exposure. b) Schematic illustration of UV light exposure through the fML array to form polymer cones and self-aligned WGs based on the different RI induced by thermal and photo crosslinking. c) Top and cross-sectional SEM images of the fML array, showing the SU-8 ML array and fML array structures with SU-8 and NOA layers. The line graph shows geometrical profile of SU-8 and NOA layers using confocal microscope. d) False-colored optical microscope images of self-aligned WG. e) Cross-sectional light intensity distribution at UV exposure doses (unexposed and 1560 mJ cm^{-2}) showing focus consistency along the increased depth. For exposure dose of 1560 mJ cm^{-2}, focus depth is extended than that of the unexposed state, indicating that self-aligned WG is formed using the UV exposure. f) 3D surface plots from confocal microscopy (640 nm laser) showing the evolution of self-aligned WG formation after 0 and 120 s of UV exposure. g) Light intensity distribution for uniformity analysis. Confocal scanning images (top row) of light intensity within the region containing MLs and WGs. The uniform distribution of light across WG input and output ports confirms the efficient guiding performance of the self-aligned WGs. h) Line graph of the effect of external RI on focal length. The cML system shows significant deviation while the fML system remains stable, demonstrating its adaptability to environmental changes (i.e., environment-adaptive WGs).

In Figure 2b, a schematic illustrates the formation mechanism of the self-aligned WG through the UV exposure process. The photosensitive polymer SU-8, used for the fML materials, guides the UV light along the optical path due to the focusing capability of the fML array. As the UV light is concentrated by each ML, the UV optical path induces localized photo-crosslinking in the SU-8, resulting in increased RI in the exposed region. This forms the polymer cone that extends to the focal point. The unexposed and thermal-crosslinked surrounding region maintains a lower RI, forming a cladding region. This RI difference between core and cladding enables optical confinement, thereby forming a self-aligned WG structure. Despite optical diffusion during exposure, this process, allows the fML array to precisely and automatically define the WG with a diameter approximately one-tenth that of the MLs without the need for additional alignment step.[11,26]

Top and cross-sectional SEM images in Figure 2c display the fML array structure with distinct SU-8 cML array and NOA flat layers, forming the MLA and WG structures. The line graph illustrates the geometrical profile of the SU-8 and NOA layers, confirming consistent thickness and alignment within the fML array. To visualize self-aligned WGs, Figure 2d presents a false-colored optical microscope image, emphasizing the clear WG structure regions formed beneath the MLs. Raw optical microscope images are presented in Figure S3 (Supporting Information). Figure 2e presents cross-sectional stacked optical microscope images showing the light intensity distribution across varying UV exposure doses (from 260 to 1560 mJ cm^{-2}). As the UV exposure dose increases, the depth and focus of the WG are extended, enhancing light guidance through the WG. At the maximum exposure dose of 1560 mJ cm^{-2}, the focus depth extends up to ≈90 μm, compared to ≈30 μm in the unexposed state, indicating the successful formation of self-aligned WGs using UV exposure. Detailed light intensity distributions for other exposure doses are provided in Figure S4 (Supporting

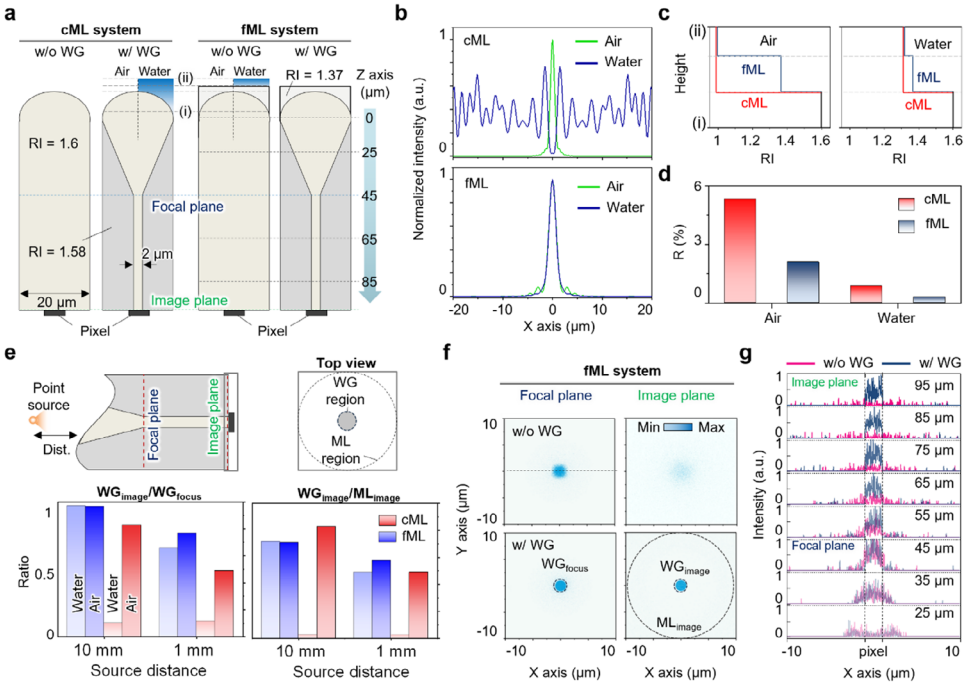

Figure 3. Amphibious optical evaluation of the artificial ommatidium integrated a self-aligned WG with fML. a) Schematic comparison of artificial ommatidia with and without a self-aligned WG at cML and fML. MLs are designed with a focal plane at Z = 45 μm and an image plane at Z = 95 μm. b) PSFs of both systems in air and underwater, demonstrating the superior focusing stability of fML system. c) Comparison of the RI profiles in air (left) and underwater (right) for the height from (i) to (ii) shown in Figure 2a. d) Reflectivity comparison for cML and fML in air and underwater. Low reflectivity in fML results from suppression of Fresnel reflection with gradual RI changes. e) Optical simulation of light intensity of focus and image planes in cML and fML with WG systems for evaluating light distribution. Top view of the cML and fML with WG systems shows WG region and ML regions. The bottom figures show comparative optical performance of the WG in the cML and fML systems for source distance of 1 and 10 mm. WG_{image}/WG_{focus} indicates the transfer rate for focusing light from focal plane to image plane. The fML system shows resistant optical performance under different external environments, while the cML system lose focus consistency in dynamic conditions. WG_{image}/ML_{image} indicates the resultant imaging efficiency in image planes, demonstrating the stability of imaging performance in the fML with WG system under multi-environmental conditions. f) Light intensity profiles showing enhanced light confinement in WG structure (bottom row) compared to system without WG (top row). g) Axial intensity profiles demonstrating efficient light trapping and propagation in the WG system (marked by dashed lines).

Information). This result demonstrates that higher UV doses increase the polymerization depth, allowing for optimized WG formation.[26]

Figure 2f shows further analysis of self-aligned WG formation using confocal microscopy with a 640 nm laser, illustrating the evolution of self-aligned WG formation over exposure time. The 3D surface plots depict the development of self-aligned WGs after 120 s of UV exposure, confirming the precise and uniform formation of WGs within the ML array. To evaluate the optical uniformity of the fabricated self-aligned WG structures, Figure 2g presents the light intensity distribution within the WG regions in Figure 2f. MLs and WGs regions are set in confocal microscope images (top row). The region-of-interest (ROI) was extracted using a MATLAB-based intensity detection algorithm. Specifically, the ROIs were defined in the focal plane by identifying regions that exceeded a certain intensity threshold, corresponding to the light-converging areas of each ML. Circular ROIs were then positioned around these intensity peaks to analyze the light intensity distribution across the WG array. The light intensity contour map of WGs (bottom row) shows the uniformity across WGs at input and output ports, indicating the uniform light-guiding performance of the self-aligned WGs. The total WG regions and sliced z-axis section are shown in Figure S5 (Supporting Information). This uniform distribution is crucial for maintaining clear imaging.

Finally, Figure 2h evaluates the effect of external RI variations on focal length stability. The cML system exhibits significant focal length deviations due to environmental changes, whereas the fML system remains stable, demonstrating its adaptability to multi-environmental conditions. This confirms that fabricating self-aligned WGs using fML array enables environment-adaptive artificial vision systems.

2.3. Comparative Environment-Adaptive Optical Performance of cML and fML Systems

Figure 3a shows a schematic comparison of the optical configurations of the artificial ommatidia for optical simulation, where both cML and fML systems are evaluated with and without a self-aligned WG for environment-adaptive optical characterization. The ML diameter is fixed at 20 μm in both systems. The cML is designed with a spherical curvature corresponding to a radius of 21 μm and the fML consisted of a two-layer structure: the first layer with a curvature of 10 μm, and the second layer with flat

surface (i.e., infinite radius). The back focal length is set to 45 μm for both cML and fML systems, and the cone height is adjusted to align the WG input port with the focal plane. The WG height ranges from 15 to 50 μm, with the WG output port aligned to the image plane. Detailed geometry and optical design parameters are summarized in Figure S6 and Table S1 (Supporting Information). The designed MLs feature a focal plane at Z = 45 μm and an image plane at Z = 95 μm, ensuring controlled optical properties for comparative analysis.

Figure 3b compares the point spread function (PSF) for the cML and fML systems across the air and underwater environments. These results demonstrate that the cML system experiences a significant loss of underwater imaging capability, resulting in a dispersed PSF profile. In contrast, the fML system maintains a sharp and well-focused PSF across the air and underwater environments, indicating that the fML design is more robust to changes in RI. Such stability suggests the fML system is better suited for applications requiring consistent, precise imaging across different media. Figure S7 (Supporting Information) shows an additional amphibious analysis of the RMS spot radius and its diagram.

The RI profiles in air and underwater for the cML and fML systems are compared in Figure 3c, where the height is set from points (i) to (ii) as indicated in the bottom-right view of Figure 3a. In the fML system, gradual RI changes help to minimize Fresnel reflections, supporting more consistent transmission performance across different media. This gradual RI transition contrasts with the sharper RI profile seen in the cML system, leading to higher Fresnel reflection and reduced optical transmittance underwater. Figure 3d shows reflectivity for the cML and fML systems, where the fML system exhibits over 50% lower reflectivity across the air and underwater environments due to the gradual RI transition. This reduction in Fresnel reflections contributes to the stable optical performance of the fML system under changing environmental conditions, an essential feature for amphibious applications.

Figure 3e provides waveguiding performance of the cML and fML with WG, a schematic illustration (top) with a comparison of the WG performance (bottom), including the focus and image planes for the cML and fML systems with WG. The point source is apart from both systems at a set distance. The top view shows the WG and ML regions within both systems, illustrating how light is distributed as it travels through these regions. Comparison of the WG performance of the WG in the cML and fML systems is evaluated for source distances at 1 and 10 mm. The ratio of WG_{image}/WG_{focus} (bottom left; Figure 3e) reflects the transfer rate of focused light from the focal plane to the image plane. The fML system shows constant optical performance across different environmental conditions, indicating consistent light transfer along the WG. In contrast, the cML system loses the WG functionality underwater. The WG_{image}/ML_{image} ratio (bottom left; Figure 3e) illustrates the imaging efficiency at the image plane, demonstrating that the fML system with WG maintains stable imaging performance across multi-environmental conditions. This result exhibits the fML system's stability and highlights its suitability for applications requiring reliable imaging in varying refractive environments. Note that light distribution profiles for source distance at 1 and 10 mm can be found in Figure S8 (Supporting Information).

The light intensity profiles for the fML system, with and without the WG, are displayed in Figure 3f. The fML without WG (top row) shows more dispersed light patterns, indicating a loss of light along the propagation path. In contrast, fML with WG (bottom row) demonstrates consistent light transfer along the WG, where light remains concentrated as it travels through the WG, highlighting its role in maintaining light integrity across depths. An additional light intensity profile along the z-axis is provided in Figure S9 (Supporting Information).

Figure 3g presents the intensity profiles along the dashed line indicated in Figure 3f, showing light propagation along the z-axis. The results reveal that in the fML system with WG, light is efficiently confined within the WG, allowing it to reach the pixel without significant loss of visual information. This effective light trapping within the WG facilitates improved imaging quality and reliability, particularly in environments where RIs may fluctuate. The dashed line marks the WG region, showing the area where light is channeled directly to the imaging plane.

2.4. Enhancement of HR ACE Vision Through Self-Aligned WG Integration

In compound eye camera systems, imaging resolution is primarily determined by the number of optical units—each comprising a ML and a set of photodetectors. Reducing the ML diameter enables higher packing density within a fixed sensor area, thereby improving spatial resolution. Integrating self-aligned WGs with fMLs enhances the ACE system's environmental adaptability and imaging resolution. The system's feasibility to precisely control ML alignment and optical parameters is crucial in achieving HR imaging. **Figure 4** presents a detailed HR imaging evaluation of the impact of self-aligned WGs on ML system design, focal length sensitivity, pixel density, and imaging resolution.

Figure 4a compares different optical configurations, illustrating that, unlike a bulky fML, a small fML without WG suffers from a non-adjustable thickness, limiting the fabrication tolerance for focal length and resulting in alignment difficulties. In contrast, integrating self-aligned WGs with small fMLs provides membrane thickness adjustability—relaxed alignment tolerance from focal plane to the image sensor plane—allowing for precise optical alignment and system miniaturization. This ability to fine-tune the optical path is particularly beneficial for ensuring consistent focal performance in high-density ML array.

As shown in Figure 4b, the focal length of a ML becomes highly sensitive in both curvatures as its diameter decreases, particularly at the microscale. This presents a significant challenge in the fabrication/integration of compact and HR imaging devices, as slight variations in membrane thickness can result in significant focal shifts. Therefore, achieving precise control over the fabrication parameters of high-density ML arrays is essential for maintaining structural stability and HR performance.

Figure 4c shows the total number of pixels within a 25 mm^2 of the sensor's area, directly correlating with the ML density. As the ML diameter decreases, the total number of pixels significantly increases in sensor area, enhancing the overall imaging resolution. A higher ML density—provided that the WG

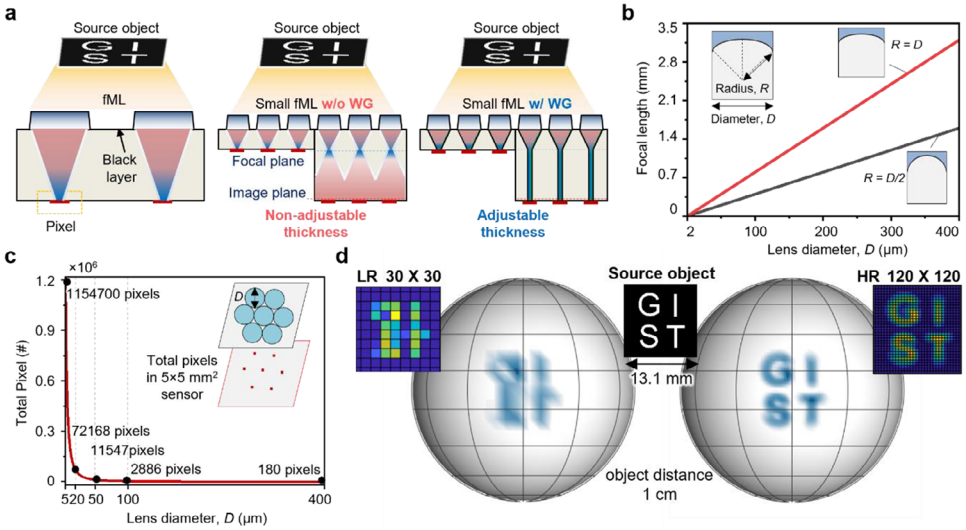

Figure 4. Enhancement of HR ACE vision system through self-aligned WG integration. a) Comparison of optical configurations show small fML without a WG has a non-adjustable thickness, leading to limitations in optical system design and challenges in well-aligned fabrication. In contrast, the integration of self-aligned WGs with small fMLs enables thickness adjustability, allowing for precise optical alignment and system miniaturization. b) Focal length variation as a function of ML diameter. As the ML diameter decreases, the focal length becomes highly sensitive on the micro-scale, making it difficult to fabricate membranes with precise thickness corresponding to the required focal length. c) Total pixel variation of high-density ML integration as a function of ML diameter. As the MLA becomes more densely packed, the total pixel count in a 25 mm^2 sensor area significantly increases, improving overall imaging resolution. d) Imaging simulation with different MLs resolutions exhibit a low-density ML array (30 × 30) results in blurred imaging due to limited pixel resolution, whereas a HR system (120 × 120) with densely integrated fMLs and WGs enables clear object reconstruction.

diameter, typically formed at 1/10 of the ML diameter,[26] remains sufficiently large to avoid substantial diffraction effects—allows for finer spatial resolution and improved image reconstruction in high-performance ACE vision systems.

Imaging simulations were conducted for different ML densities to investigate further the impact of the number of MLs on image resolution, as shown in Figure 4d. The letter object is set to a distance of 1.31 cm. Due to limited pixel resolution, a low-density ML array (30 × 30 MLs) produces mosaic and blurred images. In contrast, an HR system (120 × 120 MLs) with densely integrated fMLs and WGs achieves sharp and clear object reconstruction, demonstrating the significant enhancement in imaging quality that can be realized through ML miniaturization and WG integration. Detailed angular sensitivity analysis and simulation are discussed in Figure S10 (Supporting Information) and Experimental Section.

2.5. Optical Evaluation and Imaging Characterization of Environment-Adaptive and HR ACE

A schematic of the evaluation setup is shown in **Figure** 5a, illustrating the experimental approach used to assess the amphibious characteristics of the fML array system with a self-aligned WG. This setup enables a comparative analysis of optical stability and light intensity distribution across different environmental conditions. Figure 5b compares the light intensity distribution in fML array and cML array systems under air and underwater conditions. Unlike the cML array system, which exhibits good focusing performance in air but suffers from defocusing in water condition due to changes in the surrounding RI, the fML array system maintains stable focusing in both air and underwater environments, ensuring superior environmental adaptability.

Figure 5c analyzes light confinement and propagation, examining the effect of self-aligned WGs on light intensity distribution. Unlike the fML system without self-aligned WGs, self-aligned WGs ensure that light is effectively trapped and concentrated at the center, enhancing optical efficiency and reducing light loss to the image plane. Light intensity distribution in the focal plane and additional analysis are shown in Figure S11 (Supporting Information). This capability is critical for improving resolution and maintaining stable imaging performance in multi-environmental conditions.

An experimental setup was designed to evaluate imaging performance using object sources such as a line-pair pattern and the number "9", as shown in Figure 5d. This setup allows for a quantitative comparison of imaging capabilities across different MLs configurations. The experimental results of imaging resolution according to ML diameter are presented in Figure 5e for MLs with diameters of 400, 80, and 20 μm. The results confirm that as the ML diameter decreases, HR imaging is achieved, demonstrating the significant resolution enhancement enabled by smaller MLs. For supporting objective validation, Figures S12 and S13 (Supporting Information) present the reconstructed images and a comprehensive spatial resolution analysis. The ability to scale down the ML size while maintaining optical efficiency is a key advantage of the fML array with WG system, making it suitable for HR imaging applications.

To further investigate the environmental adaptability of the fML array system, imaging comparisons were performed between fML and cML systems with WGs in air and underwater conditions, as shown in Figure 5f. The numerical number "9" as a source object was visioned to demonstrate that the fML system

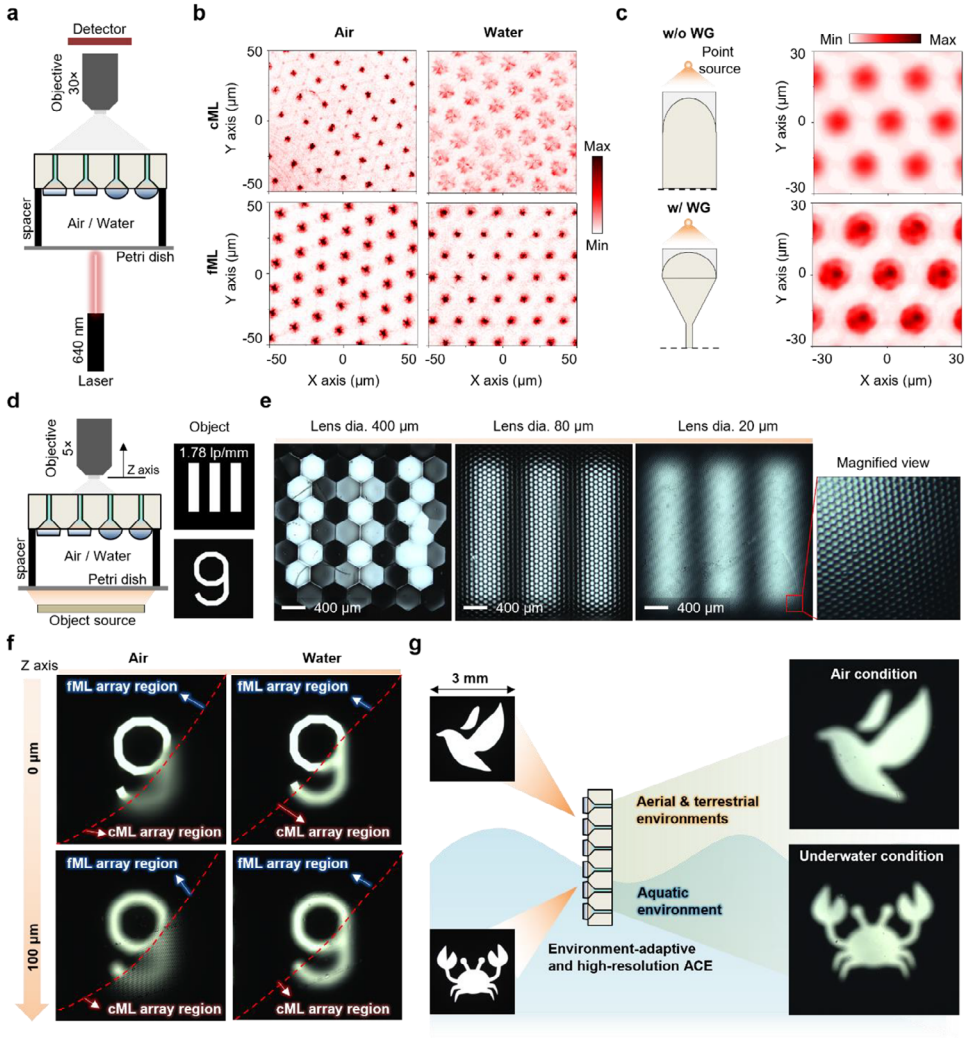

Figure 5. Optical and imaging characteristic evaluation of environment-adaptive and HR ACE. a) Schematic of the experimental setup illustrating the evaluation process of the environment-adaptive fML system with a self-aligned WG. b) Comparison of light intensity distribution. Unlike in the cML array system, where light focusing is inconsistent, the fML array system maintains stable light focusing across different environments. c) Effect of the WGs on light intensity distribution. The presence of a WG ensures that light is trapped and concentrated at the center, improving optical efficiency. d) Experimental setup for imaging performance evaluation with object sources including a line-pair pattern and the number "9", are used to evaluate the imaging performance of different ML configurations. e) Detector images at different ML diameters. Imaging results for MLs with diameters of 400, 80, and 20 μm. As the ML diameter decreases, HR imaging is achieved, demonstrating the resolution enhancement with miniaturized MLs. f) Environment-adaptive imaging comparison of fML and cML with WG. Imaging results of the number "9" as the source object across the air and underwater environments. The fML system with a WG maintains consistent imaging performance across both media, whereas the cML system exhibits inconsistent imaging results due to environmental RI changes. g) Demonstration of HR imaging in complex environments. Experimental results confirm that clear HR images are well obtained across the air and underwater environments, demonstrating the effectiveness of the fML with WG system for multi-environment vision applications.

with WG (above red dashed lines) maintains consistent imaging performance across the air and underwater environments. In contrast, the cML system (below red dashed lines) exhibits significant imaging inconsistencies due to RI variations affecting focal length variation. Further optical microscope images along the z-axis are displayed in Figure S14 (Supporting Information). These confirm that the fML-WG system is highly robust in dynamic environments, making it ideal for multi-environment vision applications.

Figure 5g presents an imaging demonstration of HR imaging with environment-adaptive vision. Our experimental results confirm that clear HR images that distinguish bird and crab objects in the air and underwater are obtained. This validates the effectiveness of the fML-WG system for multi-environmental vision with HR imaging applications. We further implemented a direct integration of the fML-WG array onto a commercial CMOS image sensor. As shown in Figure S15 (Supporting Information), a fish-shaped object was successfully captured through the CMOS-integrated fML-WG device. This result supports the potential of our system as a practical solution for miniaturized imaging modules. It also highlights the potential of environment-adaptive and HR ACE for various applications, including autonomous

navigation, underwater imaging, and bio-inspired vision systems.

3. Conclusion

This work deep dives into developing an amphibious and HR imaging capability by synergistically combining fML arrays with self-aligned WGs. Integrating these two key technologies–environmentally stable fMLs and precisely formed self-aligned WGs–enables consistent optical performances and HR imaging across different RIs. Our comprehensive optical analyses reveal that the system maintains stable focal lengths and PSFs across the air and underwater environments while achieving efficient light collection and enhanced spatial resolution through the self-aligned WGs. The simplified amphibious self-aligned WG fabrication process, achieved through controlled UV exposure using fML array, allows for scalable production of compact HR ACE, ensuring both environmental adaptability and HR imaging. Our proposed UV-curing fabrication method demonstrates scalability through its simplicity and high reproducibility. Although initial mold creation involves precision photolithography and etching, subsequent replication via UV curing significantly reduces complexity, time, and cost. Compared to alternative methods (e.g., two-photon polymerization), our technique offers better throughput, reduced cost per unit, and suitability for large-scale production. This approach not only solves the fundamental limitation of conventional cML in multi-environment applications but also provides a practical pathway for implementing HR amphibious vision systems. The demonstrated capabilities open new possibilities for applications ranging from underwater imaging and autonomous navigation to biomedical sensing, representing a significant advancement in adaptive and HR optical technologies.

4. Experimental Section

Optical Simulation for Artificial Ommatidium with Self-Aligned WG: The optical evaluation of the artificial ommatidium was conducted using Monte Carlo-based ray-tracing software (OpticsStudio 2023, Zemax LLC) to analyze and compare the performance of various components (Figure S6 and Table S1, Supporting Information). The optical properties of both cML and fML, each paired with a self-aligned WG, were simulated using Zemax software. Simulations focused on assessing the focusing performance and light-gathering efficiency of the ML in non-sequential mode. Additionally, the PSF of the fML system was evaluated in sequential mode using OpticStudio software. The fML design was specifically analyzed for its ability to maintain consistent optical performance across different RI environments (i.e., air and water). An optical system was employed with an ML diameter of 20 µm and a WG diameter of 2 µm, according to the dimensions of the fabricated self-aligned WG.

Resolution Comparison of Artificial Compound Eye Imaging Simulation: For resolution analysis, a MATLAB-based ray-tracing simulation was conducted on hemispherical ML arrays with different densities as a function of interommatidial angle. Each ML was assigned an experimentally obtained acceptance angle of 5° (Figure S10, Supporting Information), and a square object (1.31 cm × 1.31 cm) was placed 2 cm from the ML surface. Light propagation was first simulated in OpticStudio software, and the resulting ray data was exported and post-processed in MATLAB to reconstruct spatially resolved detector images.

Fabrication Process of PDMS Mold: To obtain a PDMS master mold for SU-8 cML array and fML array with optical adhesive (NOA1369, Norland Products), the PDMS mold was first fabricated, as shown in Figure S1 (Supporting Information). The process began with the fabrication of a quartz MLA mold. A quartz substrate was prepared, with Poly-Si deposited on both sides as a hard mask for the hydrofluoric acid (HF) wet etching process. The thicknesses of the Poly-Si and quartz substrate were 700 nm and 1 mm, respectively. Photolithography was then performed on one side of the Poly-Si using a photoresist (PR, AZ5214) with a hexagonal hole pattern mask. The Poly-Si was dry-etched using CF_4 gas in a reactive ion etcher (RIE) under the following conditions: CF_4 flow rate of 50 sccm, chamber pressure of 50 mTorr, RF power of 50 W, and an etching time of 70 min. Next, the sample with the patterned Poly-Si mask was immersed in an HF bath, where the HF solution etched the quartz substrate through the hole pattern (hole diameter: ≈2 µm; pitch: 20 µm). This etching was isotropic, creating hemispherical cavities from each via hole, and was carried out for 5 min. Following this, the Poly-Si layer was removed using potassium hydroxide (KOH) at 150 °C for 30 min. A final etching step was performed on the quartz in the HF bath without any masking layer for an additional 5 min to obtain an enhanced filling fraction with a large radius of curvature.[30] To create the PDMS mold, replica molding was used with the etched quartz substrate as the master mold, forming a concave lens array. Before pouring the PDMS, an anti-adhesive agent (DAIFREE GA-7550, DAIKIN, Japan) was sprayed onto the mold to facilitate release. The PDMS was cured in a convection oven at 60 °C for 90 min. After curing, the PDMS mold was coated with an additional layer of PDMS (3000 rpm, 30 s) on a hot plate and then detached from the master mold.

Supporting Information

Supporting Information is available from the Wiley Online Library or from the author.

Acknowledgements

This work was supported by the National Research Foundation of Korea (NRF) grant funded by the Korean Government Ministry of Science and ICT (MSIT) with grant no. RS-2021-NR057359 (to Y.M.S.), RS-2023-NR077254 (to Y.M.S.), RS-2024-00349776 (to G.J.L.), RS-2024-00463154 (to H.H.Y.), and RS-2025-00561110 (to H.H.Y.); the Industrial Strategic Technology Development Program funded by the Korean government's Ministry of Trade, Industry, and Energy (MOTIE) with grant no. RS-2024-00467230 (to Y.M.S.) and RS-2024-00431676 (to H.H.Y.); the Regional Innovation Mega Project through the Korea Innovation Foundation funded by the MSIT with grant no. 2023-DD-UP-0015 (to Y.M.S.); the Electronics and Telecommunications Research Institute (ETRI) Internal Project funded by the MSIT with grant no. 24YR1300 (to H.H.Y.); the AI-Based GIST (Gwangju Institute of Science and Technology) Research Scientist Project funded by the GIST in 2024 and 2025 (to H.H.Y.); the GIST Future-Leading Specialized Research Project funded by the GIST in 2025 (to H.H.Y.).

Conflict of Interest

The authors declare no conflict of interest.

Data Availability Statement

The data that support the findings of this study are available from the corresponding author upon reasonable request.

Keywords

amphibious vision, artificial compound eye, flat optics, high-resolution vision, self-aligned waveguide

Received: March 23, 2025
Revised: April 24, 2025
Published online:

[1] M. Kim, G. J. Lee, C. Choi, M. S. Kim, M. Lee, S. Liu, K. W. Cho, H. M. Kim, H. Cho, M. K. Choi, N. Lu, Y. M. Song, D.-H. Kim, *Nat. Electron.* **2020**, *3*, 546.
[2] Y. M. Song, Y. Xie, V. Malyarchuk, J. Xiao, I. Jung, K.-J. Choi, Z. Liu, H. Park, C. Lu, R.-H. Kim, R. Li, K. B. Crozier, Y. Huang, J. A. Rogers, *Nature* **2013**, *497*, 95.
[3] M. Kim, S. Chang, M. Kim, J.-E. Yeo, M. S. Kim, G. J. Lee, D.-H. Kim, Y. M. Song, *Sci. Robot.* **2023**, *8*, ade4698.
[4] M. Lee, G. J. Lee, H. J. Jang, E. Joh, H. Cho, M. S. Kim, H. M. Kim, K. M. Kang, J. H. Lee, M. Kim, H. Jang, J.-E. Yeo, F. Durand, N. Lu, D.-H. Kim, Y. M. Song, *Nat. Electron.* **2022**, *5*, 452.
[5] J. Park, M. S. Kim, J. Kim, S. Chang, M. Lee, G. J. Lee, Y. M. Song, D.-H. Kim, *Sci. Robot.* **2024**, *9*, adk6903.
[6] M. S. Kim, M. S. Kim, M. Lee, H. J. Jang, D. H. Kim, S. Chang, M. Kim, H. Cho, J. Kang, C. Choi, J. P. Hong, D. K. Hwang, G. J. Lee, D.-H. Kim, Y. M. Song, *Sci. Adv.* **2024**, *10*, adp2809.
[7] T. Nagata, M. Koyanagi, H. Tsukamoto, S. Saeki, K. Isono, Y. Shichida, F. Tokunaga, M. Kinoshita, K. Arikawa, A. Terakita, *Science* **2012**, *335*, 469.
[8] M. Garcia, T. Davis, S. Blair, N. Cui, V. Gruev, *Optica* **2018**, *5*, 1240.
[9] L. Gu, S. Poddar, Y. Lin, Z. Long, D. Zhang, Q. Zhang, L. Shu, X. Qiu, M. Kam, A. Javey, Z. Fan, *Nature* **2020**, *581*, 278.
[10] D. Keum, K.-W. Jang, D. S. Jeon, C. S. H. Hwang, E. K. Buschbeck, M. H. Kim, K.-H. Jeong, *Light: Sci. Appl.* **2018**, *7*, 80.
[11] K.-H. Jeong, J. Kim, L. P. Lee, *Science* **2006**, *312*, 557.
[12] B. Dai, L. Zhang, C. Zhao, H. Bachman, R. Becker, J. Mai, Z. Jiao, W. Li, L. Zheng, X. Wan, T. J. Huang, S. Zhuang, D. Zhang, *Nat. Commun.* **2021**, *12*, 6458.
[13] K. P. Bryceson, *J. Exp. Biol.* **1981**, *90*, 347.
[14] D.-E. Nilsson, *J. Comp. Physiol. A* **1990**, *167*, 71.
[15] G. Horváth, *J. Theor. Biol.* **1989**, *139*, 389.
[16] P. W. Hadden, J. Zhang, *Vision* **2023**, *7*, 6.
[17] A. Alkaladi, J. Zeil, *J. Comp. Neurol.* **2014**, *522*, 1264.
[18] C. Choi, M. K. Choi, S. Liu, M. Kim, O. K. Park, C. Im, J. Kim, X. Qin, G. J. Lee, K. W. Cho, M. Kim, E. Joh, J. Lee, D. Son, S.-H. Kwon, N. L. Jeon, Y. M. Song, N. Lu, D.-H. Kim, *Nat. Commun.* **2017**, *8*, 1664.
[19] H. C. Ko, M. P. Stoykovich, J. Song, V. Malyarchuk, W. M. Choi, C.-J. Yu, J. B. GeddesIII, J. Xiao, S. Wang, Y. Huang, J. A. Rogers, *Nature* **2008**, *454*, 748.
[20] Z. Rao, Y. Lu, Z. Li, K. Sim, Z. Ma, J. Xiao, C. Yu, *Nat. Electron.* **2021**, *4*, 513.
[21] K. Zhang, Y. H. Jung, S. Mikael, J.-H. Seo, M. Kim, H. Mi, H. Zhou, Z. Xia, W. Zhou, S. Gong, Z. Ma, *Nat. Commun.* **2017**, *8*, 1782.
[22] M. J. How, J. H. Christy, S. E. Temple, J. M. Hemmi, N. J. Marshall, N. W. Roberts, *Cur. Biol.* **2015**, *25*, 3069.
[23] J. Smolka, J. M. Hemmi, *J. Exp. Biol.* **2009**, *212*, 3522.
[24] G. J. Lee, Y. J. Yoo, Y. M. Song, *Appl. Spectrosc. Rev.* **2018**, *53*, 112.
[25] B. Zhang, G. Chen, M. M.-C. Cheng, J. C.-M. Chen, Y. Zhao, *OSA Contin.* **2020**, *3*, 2553.
[26] W. Wang, W. Yang, X. Mei, J. Li, X. Sun, *Opt. Express* **2021**, *29*, 3327.
[27] J. Kim, *Sci. Rep.* **2014**, *4*, 6291.
[28] Y. Zhai, J. Niu, Y. Liu, X. Chen, J. Liu, B. Yang, *Adv. Opt. Mater.* **2023**, *11*, 2300020.
[29] L. Dong, A. K. Agarwal, D. J. Beebe, H. Jiang, *Adv. Mater.* **2007**, *19*, 401.
[30] H. M. Kim, M. S. Kim, G. J. Lee, Y. J. Yoo, Y. M. Song, *Opt. Express* **2019**, *27*, 4435.